Transition to turbulence in a rotating channel

By W. H. FINLAY

Department of Mechanical Engineering, University of Alberta, Edmonton, Alberta,
Canada T6G 2G8

Direct numerical simulation is used to determine the flows that occur as the Reynolds number, Re, is increased in a plane channel undergoing system rotation about a spanwise axis. (Plane Poiseuille flow occurs for zero rotation rate and low Re.) A constant system rotation speed of 0.5, non-dimensionalized with respect to the bulk streamwise velocity and channel full width, is used throughout. The spectral numerical method solves the three-dimensional, time-dependent, incompressible Navier–Stokes equations using periodic boundary conditions in the streamwise and spanwise directions. On increasing the Reynolds number above the temporally periodic wavy vortex regime, near $Re = 4Re_c$ ($Re_c = 88.6$ is the critical Re for development of vortices), a second temporal frequency, ω_2, occurs in the flow that corresponds to slow, constant, spanwise motion of the vortices, superposed on the much faster, constant, streamwise motion of the wavy vortex waves. Curiously, ω_2 is always frequency locked with the wavy vortex frequency ω_1 for the parameter range explored, although the locking ratio varies. At the slightly higher Re of $4.1\,Re_c$, ω_2 is replaced by a new frequency ω_2' that corresponds to a modulation of the wavy vortices like that seen in modulated wavy Taylor vortex flow. However, unlike the Taylor–Couette geometry, the modulation frequency here can become frequency locked with the wavy vortex frequency. Increasing Re further to $Re = 4.2\,Re_c$ results in the appearance of a second incommensurate modulation frequency ω_3, yielding a quasi-periodic three-frequency flow, although there are only two frequencies (ω_2' and ω_3) present in the reference frame moving with the travelling wave associated with ω_1. At still higher Re ($Re = 4.5\,Re_c$), weak temporal chaos occurs. This flow is not turbulent however. Calculations of the instantaneous largest Lyapunov exponent, $\lambda(t)$, and the spatial structure of small perturbations to the flow show that the chaos is driven by spanwise shear instability of the streamwise velocity component. At the highest Re of $6.7\,Re_c$ considered, quasi-coherent turbulent boundary layer structures occur as transient, secondary streamwise-oriented vortices in the viscous sublayer near the inviscidly unstable (high-pressure) wall. Calculations of $\lambda(t)$ and the spatial structure of small perturbations to the flow show that the coherent structures are not caused by the local growth of small disturbances to the flow.

1. Introduction

When plane channel flow is rotated about a spanwise axis (cf. figure 1), streamwise-oriented vortices can develop when the Reynolds number, Re, exceeds a certain value and the rotation rate is in a certain range. At higher Re, these vortices develop waves travelling in the streamwise direction. At still higher Re, turbulence occurs. It is not known what flows occur between wavy vortices and turbulence. In this paper, direct numerical simulation is used to examine several flows that occur in this previously unexplored regime.
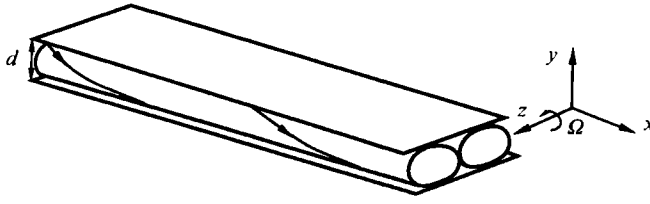
W. H. Finlay

FIGURE 1. Schematic drawing of one pair of rotating channel vortices.

The rotating channel geometry is shown in figure 1. The streamwise, normal and spanwise directions are (x, y, z) respectively. The flow is driven by a streamwise pressure gradient. The Reynolds number used here is $Re = \bar{U}d/\nu$, where $\bar{U}$ is the bulk streamwise velocity and d is the channel full width. The rotation speed Ω about the spanwise axis is non-dimensionalized to give the rotation number $Ro = \Omega d/\bar{U}$. In this paper, all lengths are non-dimensionalized by d and all velocities by $\bar{U}$, unless otherwise stated.

The rotating channel is a simplification of the geometries occurring in cooling passages within turbine blades, or the flow inside impellers of centrifugal pumps. Studying the rotating channel may thus lead to a better understanding of these flows. In addition, understanding the behaviour of vortices in the rotating channel may help unravel some of the mysteries of the streamwise-oriented vortices that occur in many flows of engineering interest.

At low enough Re, the flow in an infinite-span rotating channel is plane Poiseuille flow, with a modification of the normal pressure gradient to compensate for the Coriolis force when $Ro \neq 0$. The wall at $y = -\frac{1}{2}$ is under a higher pressure than that at $y = \frac{1}{2}$, which leads to the terms high- and low-pressure wall. For rotation rates between $0 < Ro < 3$, this flow is inviscidly unstable for $y < 0$ and thus the low-pressure wall is also called the unstable wall, and the high-pressure wall the stable wall. Viscous stability analysis shows that the entire flow is modified at high enough Re by two-dimensional streamwise-oriented vortices which span the entire gap. The term two-dimensional indicates that the flow is dependent only on two spatial coordinates (y, z), though there are three non-zero velocity components. The non-dimensional spanwise wavenumber of the vortices is $\alpha = 2\pi d/\lambda$, where λ is the spanwise vortex spacing. For given α and Ro, linear stability analysis gives the neutrally stable Reynolds number, Re_{ns}, above which two-dimensional vortices have positive linear growth rates. For given Ro, the minimum of the neutral stability curve $Re_{ns}(\alpha)$ occurs at the critical Reynolds number Re_c and the critical wavenumber α_c. For $Ro = 0.5$ used here, $Re_c = 88.60$ and $\alpha_c = 4.91$. For $Re > Re_c$ two-dimensional vortices can occur. This transition is supercritical. Previous authors have dealt with the transition from one-dimensional flow to two-dimensional vortices (Finlay 1989; Alfredsson & Persson 1989; and see Tritton & Davies 1985 for less recent work).

At higher Re, two-dimensional vortices become unstable to waves that travel in the streamwise direction at constant speed. This transition appears to be a supercritical Hopf bifurcation and the resulting wavy vortices have been noted experimentally (Alfredsson & Persson 1989; Kuz'minskii, Smirnov & Yurkin 1983; Smirnov & Yurkin 1983) and examined numerically (Finlay 1990; Yang & Kim 1991).

In the experiments of Alfredsson & Persson (1989), the vortices appear turbulent at Re well below that required for turbulence in the non-rotating plane channel. The flows leading up to this low-Re turbulence and the processes responsible for sustaining

it are unknown. In this study, the flow regimes from wavy vortices to low-Re turbulence are examined. In §2 the numerical method is briefly described and the limitations of the spatially periodic boundary conditions being used are also briefly mentioned. In §3 a flow is discussed in which the vortices travel slowly in the spanwise direction. Quasi-periodic flows with two and three frequencies are discussed in §4. A weakly chaotic flow is found in §5, and the physical mechanism causing this chaos is discussed in §6. Low-Re turbulence is discussed in §7. Concluding remarks are given in §8.

2. Numerical method

Using the numerical method of Moser, Moin & Leonard (1983), three-dimensional time-dependent solutions of the incompressible Navier–Stokes equations for a rotating channel are obtained. Periodic boundary conditions are used in the spanwise and streamwise directions. A Galerkin pseudo-spectral method based on expansion functions that satisfy the continuity equation and the boundary conditions is used. Time-advancement is implicit (Crank–Nicholson) for viscous terms and explicit (second-order Adams–Bashforth) for nonlinear and Coriolis terms. The solution progresses in time with constant mass flux imposed. The number of modes in (x, y, z) is $32 \times 20 \times 20$. Spatial energy spectra are monitored to ensure that energy decreases exponentially with increasing Fourier wavenumber and thus that adequate resolution is being used. To eliminate aliasing errors, the nonlinear terms are evaluated in real space on a grid with $\frac{3}{2}$ as many grid points in each direction as the number of modes used in transform space (cf. Canuto *et al.* 1988). The code is a modification of the one used to study wavy vortices in the rotating channel by Finlay (1990).

Two different sets of initial conditions are used: one consists of low-amplitude $(0.001 \% \, \bar{U})$ random noise superposed on a lowest-order approximation to two-dimensional vortices; the other consists of the equilibrium solution from a lower Re. Both sets of initial conditions give the same equilibrium solution.

Owing to long transients in several of the simulations, only a limited parameter range is explored. A rotation number $Ro = 0.5$ was chosen since this is the value with the lowest Re for the onset of two-dimensional vortices from rotating plane Poiseuille flow. In comparison with other Ro, it was hoped that subsequent transitions would also occur at comparatively low Re. Spanwise wavenumbers in the range $\alpha = 5.9$ to 6 were used since this is near the experimental values observed by Alfredsson & Persson (1989) and is also near the Eckhaus valley (Guo & Finlay 1991), so that vortices with this wavenumber are likely to exist for long times without having their wavenumbers affected by splitting or merging of vortex pairs. The streamwise extent of the computational region is $\mu = 2\pi/\beta$ and was between 3.7 and 4 times the spanwise extent, since this corresponds approximately to the most unstable wavelength for wavy vortices with the given Ro and α. The streamwise wavelengths of the waves shown in flow visualizations by Alfredsson & Persson (1989), and Matsson & Alfredsson (1990) at lower Ro are comparable to those of the most unstable mode.

The use of periodic streamwise boundary conditions implies that the flow is fully developed, i.e. the flow is at a streamwise position beyond its development length. In the aspects just mentioned, periodic boundary conditions cannot produce an exact replica of an experimental configuration; however, such boundary conditions have successfully simulated many of the essential features of complex flows in a large

number of different geometries with only a small segment of the flow pattern simulated (see for example, Kleiser & Zang 1991; Jiménez & Moin 1991; Biringen & Peltier 1990; Tryggvason & Unverdi 1990; Jiménez 1990; Malik & Hussaini 1990; Herbert 1988; Hall 1988). Many useful results can be obtained in this manner, and the present geometry is no exception.

3. Slow spanwise travelling of wavy vortices

For $Ro = 0.5$, $\alpha = 6$, and $\beta = 1.5$ the transition from rotating plane Poiseuille flow to two-dimensional vortices occurs at $Re_{ns} = 1.030\,Re_c$. The transition from two-dimensional vortices to wavy vortices occurs at $Re'_{ns} = 3.0\,Re_c$. Wavy vortices are temporally periodic and are due to travelling waves in which the flow pattern travels with uniform streamwise velocity c_1. Specifically, the velocity v satisfies

$$v((x+c_1\,\Delta t)\,\mathrm{mod}\,2\pi/\beta, y, z, t + \Delta t) = v(x, y, z, t). \tag{1}$$

Experimentally, merging and splitting events, as well as the convective nature of the channel and the continually varying inlet conditions prevent wavy vortices from being exactly periodic in time or space. Numerically simulated wavy vortices with periodic boundary conditions also have shift-and-reflect symmetry (Finlay 1990):

$$\left.\begin{aligned}
v_y(x, y, z, t) &= v_y(x+\pi/\beta, y, -z, t), \\
v_x(x, y, z, t) &= v_x(x+\pi/\beta, y, -z, t), \\
v_z(x, y, z, t) &= -v_z(x+\pi/\beta, y, -z, t),
\end{aligned}\right\} \tag{2}$$

where $z = 0$ is the average location of an upflow or downflow plane and $v = (v_x, v_y, v_z)$. Experimental channels have finite length, which removes this symmetry. Thus any bifurcations associated with the streamwise direction will be imperfect, just as the finite span causes the transition from Poiseuille flow to two-dimensional vortices to be imperfect (Finlay & Nandakumar 1990).

Figure 2 shows a time record and power spectrum of the velocity sampled at one point in the flow from a simulation at $Re = 3.2\,Re_c$. (Throughout this paper the power spectra shown at various Re are qualitatively independent of the sampling position in the flow.) This run was started from the random initial conditions discussed in §2. To obtain figure 2 the velocity was sampled every 20 time steps in the simulation (one time step is $0.015d/\bar{U}$), which gives a slightly jagged appearance to the data in figure 2(a). After an initial transient, the flow reaches a wavy vortex state (WVF1) like that described by Finlay (1990). The flow is temporally periodic with fundamental frequency $\omega_1 = 1.32 \pm 0.01$ (or period $T_1' = 2\pi/\omega_1$); five harmonics of the fundamental are labelled in figure 2(b). Equation (1) implies that the wave travels at streamwise speed $c_1 = \omega/\beta$. Time records taken in a frame moving at this speed are steady, verifying the travelling wave nature of the flow.

When the Reynolds number is increased to $Re = 4Re_c$, time series show the appearance of a second low frequency. The oscillation due to the wavy vortices is now modulated at very low frequency ω_2. Figure 3(a) shows a time record of v_z sampled every ten time steps at one point in the flow once the flow has essentially reached its equilibrium state. This run was started from the equilibrium solution at $Re = 3.2\,Re_c$. For clarity, only the low-frequency portion of the power spectrum associated with this time record is shown in figure 3(b). (The higher-frequency portion is similar to that in figure 2(b) except for the appearance of sidelobes on each harmonic due to ω_2.)
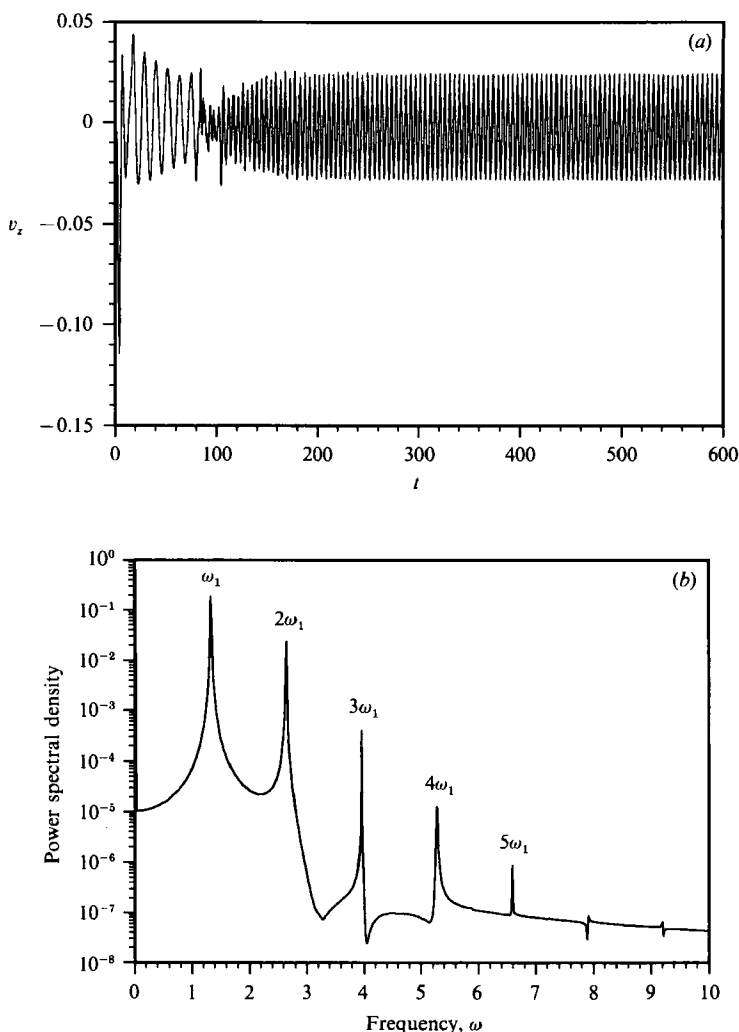
FIGURE 2. (a) Time series and (b) power spectral density of v_z for temporally periodic wavy vortices at $Re = 3.6Re_c$ sampled at one point in the flow. The power spectral density (also called the power spectrum, autospectral density, or autospectrum) of $v_z(t)$ is taken from the data in (a) for $t > 300$ where the initial transient non-periodic behaviour has decayed to an insignificant level.

The rapid oscillations in figure 3(a) are due to the wavy vortex frequency $\omega_1 = 1.32 \pm 0.01$. The low-frequency, amplitude modulation of the signal in figure 3(a) is at a frequency $\omega_2 = 0.0113 \pm 0.0002$. The period associated with ω_2 is $T_2 = 2\pi/\omega_2$. Because there are now two frequencies in the flow, power spectra have peaks at integer combinations of the two fundamental frequencies. (The very low-amplitude peak near $\omega = 0.63$ in figure 3(b) is a transient frequency which is not present in spectra obtained at later times.) In figure 3(b), the frequencies $\omega_1 - m\omega_2$ for $m = 0, 1, 2$ and $n\omega_2$ for $n = 1, 2$ contain all of the significant energy.

By measuring the time between successive minima or maxima due to the wavy vortices in figure 3(a) one obtains the time required for one wavelength of the wavy vortex to pass by in the streamwise direction. The time between waves was measured over a duration $6T_1$ near two times separated by approximately $\frac{1}{2}T_2$. The difference between the longest and shortest times between successive waves over these times
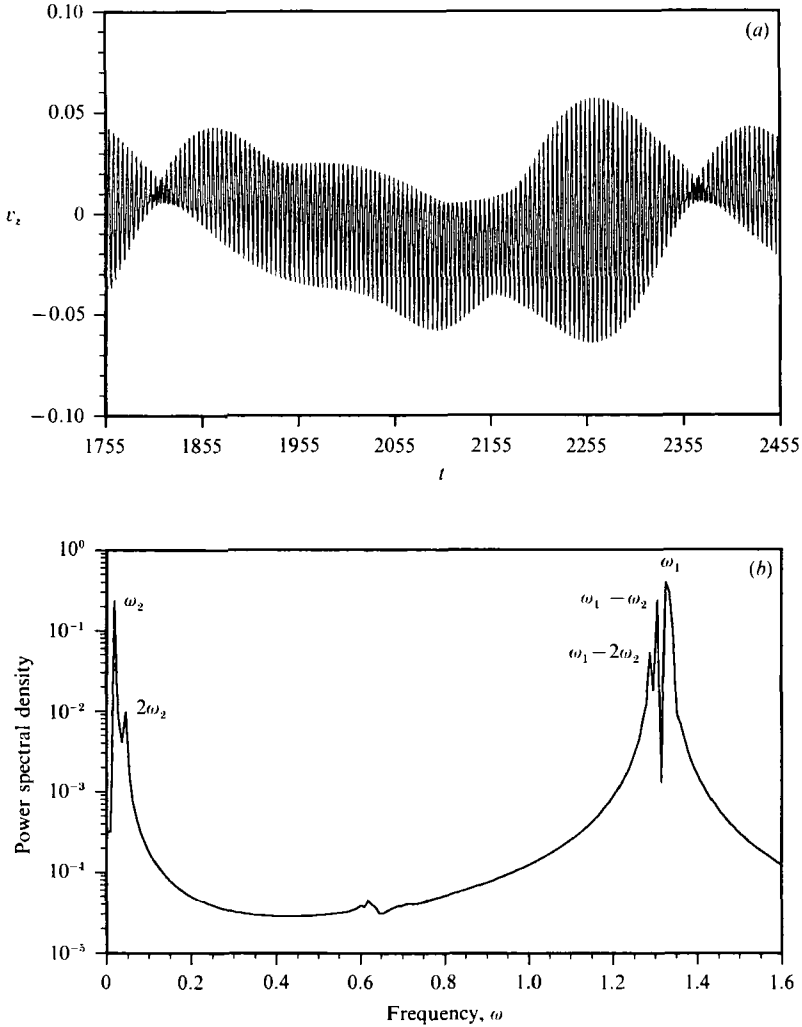
FIGURE 3. (a) Time series and (b) power spectral density of v_z for spanwise travelling wavy vortices at $Re = 4\,Re_c$ sampled at one point in the flow. The data in (b) show only the low-frequency portion of the full power spectrum associated with (a).

was $0.028T_1 \pm 0.005T_1$, indicating that ω_2 causes frequency modulation. Thus, the signal in figure 3(a) is modulated both in frequency and amplitude by ω_2.

When two frequencies occur in a dynamical system it is common for the ratio of the two frequencies to become locked at a rational number over a certain range of the dynamical parameter (Bergé, Pomeau & Vidal 1984). This phenomenon is called frequency locking, phase locking, or entrainment. The system is periodic in time when frequency locking occurs. At $Re = 4\,Re_c$, close examination of time series shows that the flow is periodic in time with period ω_2 and that $\omega_1 = 117\omega_2$. For example, the low-amplitude portion of the signal near the left side of figure 3(a) is separated by T_2 from an identical low-amplitude portion near the right side. This is best seen if only part of figure 3(a) is drawn and then superimposed on the signal at a time T_2 later. There is no visible difference between the two signals when superimposed in this manner, indicating the flow is periodic with period T_2. The wavy vortex frequency ω_1 is frequency locked with the frequency ω_2 in the ratio 117/1.

In other dynamical systems, frequency locking occurs after the dynamical system has passed through a quasi-periodic regime where the two frequencies are not locked (Gollub & Benson 1980; Bergé *et al.* 1984). Thus, it may be that ω_2 is an incommensurate frequency at some Re not considered here. In most dynamical systems, the two frequencies remain locked at certain rational numbers over a range of the dynamical parameter. Thus at Re slightly higher or lower than $4Re_c$ one might expect ω_1/ω_2 still to be locked in the ratio $117/1$. Simulations at other Re near $4Re_c$ show frequency locking; however, the ratio of ω_1/ω_2 varies rapidly with Re. Several runs with Re within 3% of $4Re_c$ all yielded frequency locked flows, but ω_1/ω_2 increased by 15% as Re increased through this range. Frequency locking has been observed in other fluid systems (e.g. Olinger & Sreenivasan 1988), and occurs in other dynamical systems, for example the circle map (Arnold 1965). In the system described by the circle map, the two frequencies become locked together over a range whenever their ratio is near a rational number. Similar behaviour has been observed experimentally in the wake of an oscillating cylinder by Olinger & Sreenivasan (1988), although the locking ratio is not so large as observed here. Similar behaviour may occur for the frequency locking observed here, i.e. the flow may remain locked at a fixed ratio over a small but finite range of Re near each of the Re considered here. This frequency locking is not an artifact of initial conditions, or the parameter set, since ω_2 is found to be frequency locked when either set of initial conditions mentioned in §2 is used, and when each of Re, α, and β is varied by several percent.

Rand (1982) has shown that it is impossible for a wavy vortex frequency to become locked with the modulation frequency associated with modulated wavy vortex flow in Taylor–Couette flow. A similar result may be shown for curved channel flow. Physical and numerical experiments in these two geometries have found no indication of frequency locking with the wavy vortex frequency (Fenstermacher, Swinney & Gollub 1979; Bland & Finlay 1991). Symmetries associated with the curved geometry are responsible for the absence of frequency locking. These symmetries are not present in the rotating channel and thus the wavy vortices can frequency lock with a modulation frequency. Such frequency locking is also observed in Rayleigh–Bénard convection (Gollub & Benson 1980).

The physical nature of the modulation due to ω_2 can be determined by observing the flow at different times over the period of one modulation. Observations were made over one period T_2 at time intervals separated by $\frac{1}{10}T_2$. The vortices are found to travel in the positive spanwise direction at constant speed $c_2 = \omega_2/\alpha$. (Since the physics are unchanged by the reflection $z \to -z$, spanwise travelling in the negative z-direction can also occur.) The original travelling waves continue to move in the streamwise direction at speed $c_1 = \omega_1/\beta$. Thus the flow at one time, t, is identical to that at a later time, $t + \Delta t$, except that the flow pattern is shifted in the spanwise and streamwise directions. The flow is steady in a reference frame that moves with a velocity having streamwise component c_1 and spanwise component c_2. Specifically,

$$v((x + c_1\Delta t) \bmod 2\pi/\beta, y, (z + c_2\Delta t) \bmod 2\pi/\alpha, t + \Delta t) = v(x, y, z, t). \tag{3}$$

Because ω_2 and ω_1 are frequency locked at the ratio n, the travelling waves due to ω_1 move downstream a distance $n2\pi/\beta$ during the time which the vortices move in the spanwise direction a distance $2\pi/\alpha$. The spanwise velocities c_2 observed here are roughly $1/400$ times the streamwise velocities c_1. Since c_1 is of the same order as the bulk streamwise velocity (Finlay 1990; Alfredsson & Persson 1989), spanwise travelling wavy vortices would only travel one channel width in the spanwise direction in a streamwise distance of the order of 400 channel widths.
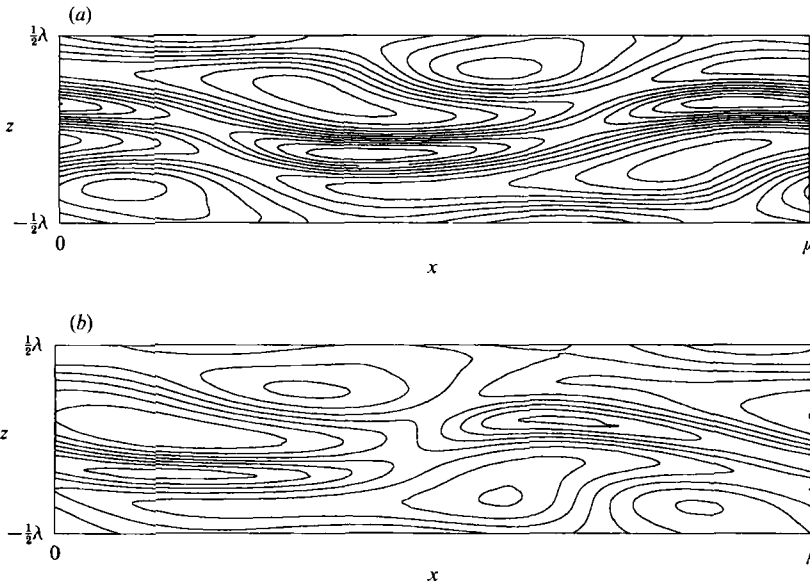
W. H. Finlay

FIGURE 4. Instantaneous contours of streamwise velocity v_x in an (x, z)-plane at the channel centreline ($y = 0$) show the shift-and-reflect symmetry of (a) wavy vortices at $Re = 3.6Re_c$, and (b) the asymmetry of spanwise travelling vortices at $Re = 4Re_c$. The contours in (a) are from 1.27 to 1.39 in increments of 0.012, while those in (b) are from 1.25 to 1.39 in increments of 0.02.

When the vortices are observed in cross-section (in a y, z-plane) at successive instants in time, the qualitative appearance of this flow differs little from the wavy vortex flows occurring at lower Re at this Ro, α, β and described by Finlay (1990). However, the flow is no longer shift-and-reflect symmetric. The appearance of ω_2 is thus symmetry breaking. This is most easily seen when contours of the velocity are plotted in an (x, z)-plane. Figure 4 (a) shows contours of the streamwise velocity v_x at $y = 0$ and one instant in time for a wavy vortex flow at $Re = 3.2Re_c$. One spanwise period λ and one streamwise period $\mu = 2\pi/\beta$ are shown. The shift-and-reflect nature of the flow is apparent; if the entire plot is shifted in the x-direction half a wavelength and then reflected about the average z-location of the upflow region (the plot is drawn so that this is $z = 0$) one obtains the same plot shown. Figure 4 (b) shows v_x at $y = 0$ for $Re = 4.063Re_c$. This flow is not shift-and-reflect symmetric.

Spanwise travelling of vortices has been observed in the swept-wing geometry (cf. Reed 1988). Whether spanwise travelling in the rotating channel is confirmed experimentally remains to be seen, since very low drift speeds, continually varying inlet conditions in experiments coupled with the convective nature of channel flow, and fixed endwalls could make this flow pattern experimentally elusive.

4. Two- and three-frequency modulated wavy vortices

As the Reynolds number is increased further, time records and power spectra show that spanwise travelling of the vortices is not present in the equilibrium flow. Instead, near $Re = 4.1Re_c$, ω_2 is replaced by a new, much higher frequency in the flow. At slightly higher Re ($Re = 4.2Re_c$), another incommensurate frequency appears, resulting in a three-frequency quasi-periodic flow. Figure 5 shows a power spectrum from a simulation at $Re = 4.3Re_c$ using $Re = 3.2Re_c$ as initial condition. The maximum frequency shown in figure 5 is only one quarter of the sampling
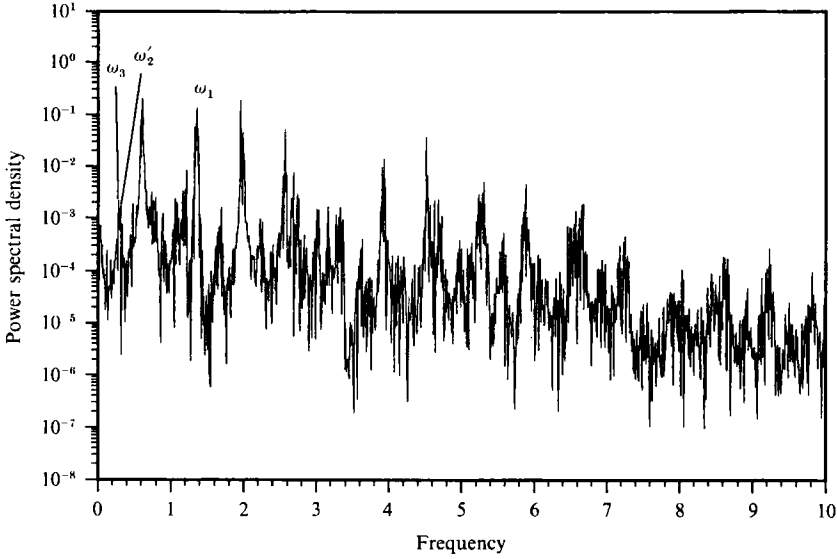
FIGURE 5. Power spectral density of v_z for three-frequency modulated wavy vortices at $Re = 4.3Re_c$ sampled at one point in the flow. The flow had reached its equilibrium state prior to sampling.

frequency, f_s. The frequency associated with the wavy vortices is apparent as $\omega_1 = 1.35 \pm 0.01$. The two other fundamental frequencies in the flow are $\omega_2' = 0.304 \pm 0.006$ and $\omega_3 = 0.278 \pm 0.006$. The first harmonics of ω_2' and ω_3 are seen as the most energetic frequencies in figure 5. Both ω_2' and ω_3 vary by less than 5% when Re is varied by $\pm 2\%$ about $Re = 4.2Re_c$. With the plot resolution used in figure 5, ω_2' and ω_3 do not appear distinct, but they are clearly distinct in the data and in higher-resolution plots. Although it is not visually apparent, all spikes in figure 5 are integer multiples of the three frequencies ω_1, ω_2' and ω_3. It is easier to discern the three-frequency character of the flow from power spectra of the pressure gradient parameter Δp, defined as

$$\Delta p \equiv \frac{(\overline{\partial p/\partial x}) - (\partial P/\partial x)}{\partial P/\partial x}, \tag{4}$$

where $\partial p/\partial x$ is the streamwise pressure gradient, $\overline{\partial p/\partial x}$ is the value of $\partial p/\partial x$ averaged over the computational box, and $\partial P/\partial x$ is the streamwise pressure gradient for Poiseuille flow. (The quantity Δp plays a role similar to that of the Nusselt number in Rayleigh–Bénard convection, or the non-dimensional torque in Taylor–Couette flow.) Owing to its travelling wave nature, ω_1 is absent from time records of Δp (or any other axisymmetric quantity) making it considerably easier to verify that there are two incommensurate frequencies besides ω_1. Figure 6 shows a spectrum for Δp (for clarity only the low-frequency portion of the spectrum is shown) corresponding to the same simulation as figure 5. Since Δp is a measure of the strength of the vortices (Finlay, Keller & Ferziger 1988), the modulation of Δp by ω_2' and ω_3 causes modulation of the strength of the vortices. All peaks in the full power spectrum are at frequencies, ω, that are linear combinations of the fundamental frequencies ω_2' and ω_3, i.e. $\omega = n\omega_2' + m\omega_3$ where n and m are integers. Most of the peaks are separated by $\omega_3 - \omega_2'$. One could alternatively choose some combination of ω_2' and ω_3 as one of the two fundamental frequencies.
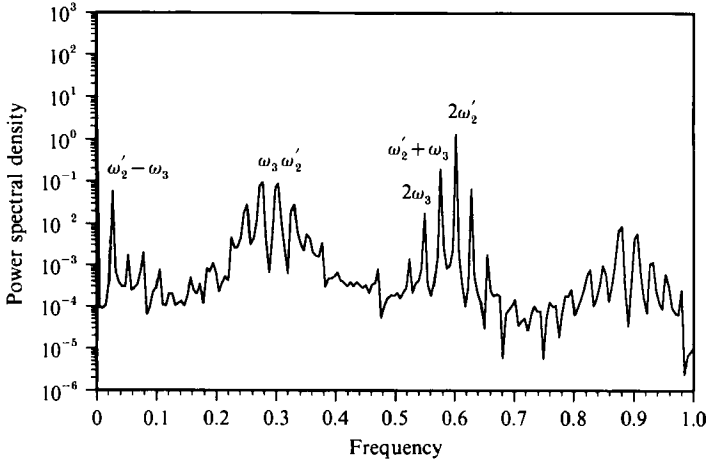
FIGURE 6. Power spectral density of Δp at $Re = 4.3 Re_c$. The flow had reached its equilibrium state prior to sampling.

The time records associated with figures 5 and 6 and similar results obtained at lower Re when ω_3 is absent show that both ω_2' and ω_3 produce amplitude modulation of the travelling wave signal. In addition, observations of the time taken for successive travelling waves to pass by show that both ω_2' and ω_3 cause variations in the temporal period, and thus the frequency, of the travelling wave. The maximum variation of the wavy vortex period observed during a time $10T_2'$ (where $T_2' = 2\pi/\omega_2'$) is approximately $0.08T_1 \pm 0.03T_1$. (Owing to the periodic streamwise boundary conditions of fixed streamwise length, such variations in the frequency of the travelling wave correspond to variations in the speed c_1 of the wave.) Thus, ω_2' and ω_3 both cause frequency and amplitude modulation.

For a small range of Re near $4.1 Re_c$ below the onset of ω_3, only ω_1 and ω_2' are present, and the flow is periodic when observed in a frame of reference moving with the streamwise speed c_1 equal to the speed of the travelling wave associated with ω_1. In such a moving frame the character of the modulation frequency ω_2' can be represented using a mathematical framework developed by Coughlin (1990) for modulated wavy Taylor vortices (see also Coughlin & Marcus 1992a, b). Coughlin (1990) performed numerical simulations of modulated wavy Taylor vortices (for a radius ratio of 0.875) using periodic boundary conditions like those used here and described the modulation frequency in terms of the following framework. For a given y and z, an arbitrary flow quantity Q depends on x and t as follows for modulated wavy vortex flow with one modulation frequency:

$$Q = \sum_j \sum_k a_{jk} \mathrm{e}^{\mathrm{i}j\beta(x - c_1 t)} \, \mathrm{e}^{\mathrm{i}k\gamma(x - c_2 t)}, \tag{5}$$

where c_1 and β are the frequency and streamwise wavenumber of the travelling wave. The modulation is characterized by a streamwise wavenumber γ and the parameter c_2, which is defined as $c_2 = c_1 + \omega_2'/\gamma$. Since the flow is temporally periodic when viewed in the travelling wave reference frame, the time-average of Q is easily obtained in the moving frame as

$$\bar{Q} = \frac{1}{T_2'} \int_0^{T_2'} Q(\hat{x}, t) \, \mathrm{d}t \tag{6}$$

where $\hat{x} = x - c_1 t$. The velocity field associated with the modulation, defined as $\boldsymbol{v}_m$, is then obtained by subtracting the time-average field in the travelling wave frame from the instantaneous field in the inertial frame, i.e.

$$\boldsymbol{v}_m = \boldsymbol{v} - \bar{\boldsymbol{v}}. \tag{7}$$

The velocity field $\boldsymbol{v}_m$ then shows a $2\pi/\beta$-periodic function modulated by a function with wavelength $2\pi/\gamma$, from which γ can be obtained. For all modulated wavy vortex flows observed here, it is found that $\gamma = \beta$.

Coughlin (1990) shows that the behaviour of $\boldsymbol{v}_m$ as a function of time demonstrates the meaning of c_2, since in the travelling wave frame the modulation is approximated by another travelling wave with an average drift speed $c_d = c_2 - c_1$. Thus the structure of the modulation is seen to drift relative to the c_1-frame at speed c_d. (The modulation cannot be characterized solely as a second travelling wave, since there is distortion of the modulation structure as it travels downstream.) For the two-frequency modulated wavy vortex flows observed here $c_d = \omega_2'/\beta \approx \frac{1}{4}c_1$.

Coughlin (1990) finds two types of modulated wavy Taylor vortices that are of interest here: ZS modulated waves and GS modulated waves. Both can be described by the above framework, but GS modes cause large-amplitude modulations of the S-shaped boundary between vortices and have $c_d \approx \frac{1}{3}c_1$, whereas ZS modes cause little change in the shape of the boundary between vortices and have $c_d \approx 2c_1$. The modulation due to ω_2' observed here is closer in character to the GS modes in that ω_2' causes large variations in the boundary between vortices and $c_d \approx \frac{1}{4}c$. However, one of the features of GS modes is that the quasi-periodic field $\boldsymbol{v}_m$ is concentrated on the sides of the outflow (upflow) region, whereas ZS modes are concentrated in the outflow (upflow) region. In this feature, ω_2' is like the ZS modes, since plots of the energy of $\boldsymbol{v}_m$ show that most of the energy of $\boldsymbol{v}_m$ is concentrated in the upflow region, not on the sides of the upflow region. Thus, the modulation due to ω_2' corresponds to neither the ZS or GS modes observed by Coughlin (1990), but it can be described by equation (5) which was developed by Coughlin (1990).

One aspect of modulated wavy vortices in the rotating channel which cannot occur in Taylor–Couette flow is frequency locking of the modulation frequency with the wavy vortex frequency, as mentioned in §3. Here it is found that the wavy vortex frequency, ω_1, and the modulation frequency ω_2' lock into the ratio 4/1 when $\alpha = 5.9$, $\beta = 0.8$, $Re = 4 Re_c$. Such locking can occur because the symmetries associated with the curve Taylor–Couette geometry are not present in the rotating channel.

For $Re > 4.2 Re_c$, the flow in the c_1-frame becomes quasi-periodic, instead of periodic, owing to the appearance of ω_3 and it is more difficult to discern the behaviour of ω_2' and ω_3 independently. The physical character of ω_2' and ω_3 is seen by observing the flow at various times. The only striking qualitative change that ω_2' and ω_3 appear to produce in the travelling wave is a modulation of the S-shape of the upflow region when viewed in an (x, z)-plane. Figure 7 shows contour plots of v_x at $y = 0$ at times separated by $0.225 T_2'$. The upflow region is located in the S-shaped low-v_x valley near $z = 0$. The S-shape is flattened by roughly 50% at the later time (b) in comparison to the earlier time (a). The S-shape of the travelling waves is maximally flattened approximately when the waves have maximum streamwise velocity, and it is maximally enhanced approximately when the waves have their slowest velocity. (This is opposite to the behaviour of modulated wavy Taylor vortex flow, cf. Gorman & Swinney 1982.) The waves also usually travel slowest at times near where there is a local minimum in the time record of Δp, and fastest at times near when there is a local maximum in Δp. Figure 7(a) is at a time when there is a
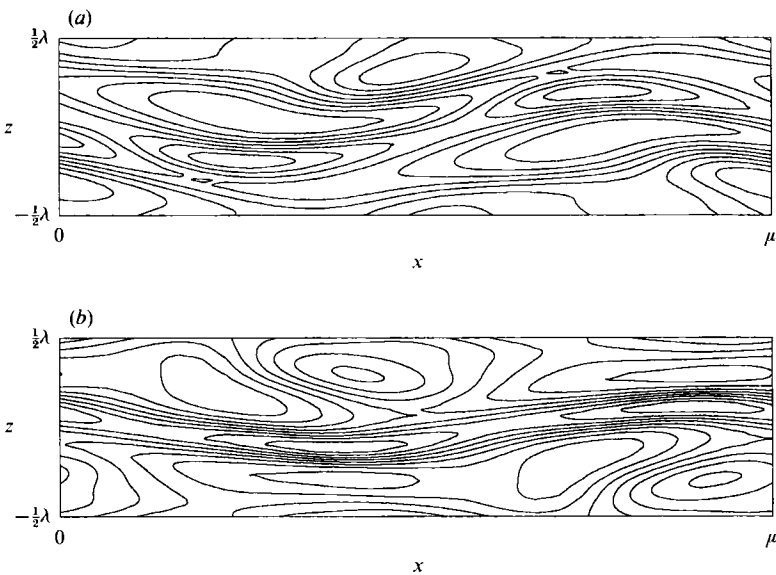
FIGURE 7. Contours of streamwise velocity v_x in an (x, z)-plane at $y = 0$ are shown
for $Re = 4.3 Re_c$ at (a) $t = 1071.4$, (b) $t = 1076.1$.

local minimum in Δp, while figure 7(b) is at the time of the following local maximum in Δp. Observations of the flow in cross-section show no other significant qualitative differences from the wavy vortex flow WVF1 shown by Finlay (1990) at $Re = 3.2 Re_c$.

As can be seen in figure 7, the flow has regained its shift-and-reflect symmetry. This symmetry was broken by the spanwise travelling mode at lower Re, but there is now no spanwise travelling of the vortices. Initial conditions which were not shift-and-reflect symmetric produced long transients during which a spanwise travelling mode slowly decayed. Conversely, the use of initial conditions that are shift-and-reflect symmetric for simulations near $Re = 4 Re_c$, where the asymmetric spanwise travelling mode is an equilibrium solution, require long transients prior to the onset of the equilibrium flow.

5. Weak chaos

Increasing Re to $4.5 Re_c$ yields a flow that is weakly chaotic. Figure 8 shows the low-frequency part of a power spectrum of v_z. This run was started from the random initial conditions discussed in §2. Three fundamental frequencies are still present in spectra, but there are many energetic peaks occurring at frequencies other than low-order combinations of these three frequencies. At $Re = 4.3 Re_c$ all peaks in the non-chaotic spectrum occur at low-order integer combinations of the three fundamental frequencies. (This difference between figures 5 and 8 is not obvious simply from visual inspection.) The three fundamentals in figure 8 are $\omega_1 = 1.33 \pm 0.01$, $\omega_2' = 0.31 \pm 0.01$ and $\omega_3 = 0.28 \pm 0.01$. One could attempt to explain the spectra using four or more fundamental frequencies, but there are no energetic frequencies in figure 8 to choose as fundamentals that would produce the peaks shown using only low-order integer combinations.

Since the travelling wave frequency ω_1 is absent from time series of the pressure gradient parameter, Δp, it is easier to identify the modulation frequencies in the Δp
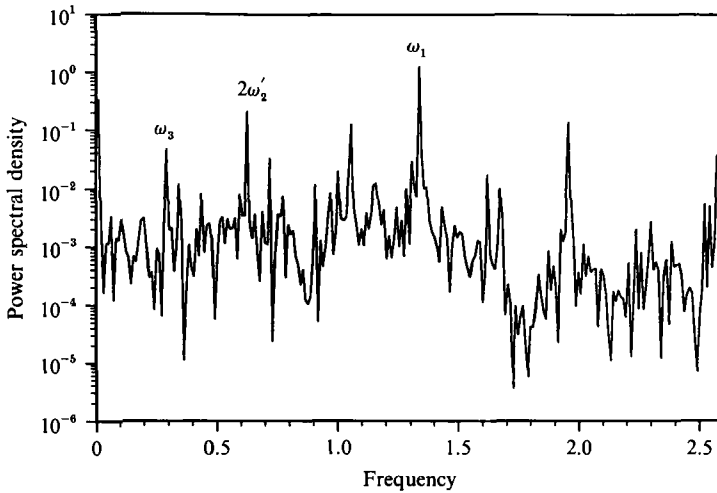
FIGURE 8. Power spectral density of v_z for chaotic modulated wavy vortices at $Re = 4.5Re_c$ sampled at one point in the flow.
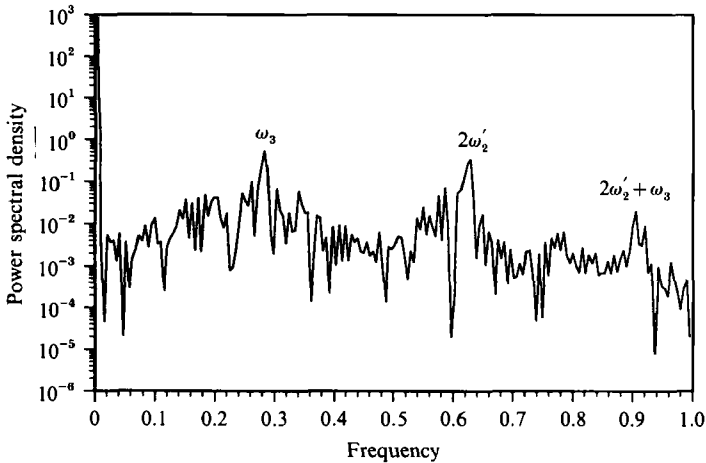

FIGURE 9. Power spectral density of Δp at $Re = 4.5Re_c$.

data shown in figure 9. Figure 9 shows there is significant energy at many frequencies other than combinations of ω_2' and ω_3, indicating the flow is chaotic in time.

Despite the occurrence of temporal chaos at $Re = 4.5Re_e$, the spatial structure of the flow at any instant remains non-turbulent. In fact, the flow is still shift-and-reflect symmetric. (The small amount of asymmetry seen for this flow in figure 12 is due to the decaying asymmetric initial conditions and is not present at later times or when symmetric initial conditions are used.) At any instant, the flow is qualitatively unchanged from that prior to the onset of temporal chaos and is similar to the wavy vortices described by Finlay (1990). The S-shape of the upflow boundary between vortices is modulated in time by the two modulation frequencies. Because of the weak temporal chaos the S-shape is also enhanced and flattened in a weakly chaotic manner.

In a reference frame travelling at the speed $c_1 = \omega_1\beta$ only two frequencies are present for all Re examined just below the onset of chaos. Thus the transition to

chaos here appears to occur directly from a T^2−torus; however, this cannot be stated unconditionally since there may exist Re ($4.4\,Re_c < Re < 4.5\,Re_c$) for which another frequency appears in the flow to yield a T^3-torus between the finite number of Re values explored.

6. Chaos driven by shear instability

In this section small perturbations to the temporally chaotic flow at $Re = 4.5\,Re_c$ are shown to grow only in regions near where the streamwise velocity component has largest spanwise shear, indicating that the chaos is driven by shear instability of these regions.

In dynamical systems the largest Lyapunov exponent, λ, gives the average exponential rate at which two nearby trajectories diverge from each other in phase space. If the Lyapunov exponent is positive then a small perturbation to the flow at one point in phase space will diverge exponentially away from the unperturbed trajectory until the two trajectories are no longer nearby. This results in chaos, since any two initial conditions that are close together will diverge exponentially, producing entirely different flows at sufficiently later times. The transition to chaos as a dynamical parameter (e.g. the Reynolds number) is varied is thus marked by the largest Lyapunov exponent passing through zero. Unfortunately, existing methods for calculating λ from solutions of the governing equations require extremely long time histories of the flow when λ is near zero. This is because the instantaneous rates of divergence of nearby trajectories usually oscillate significantly about zero, and a very long time average is needed to accurately determine the average rate of divergence given by the largest Lyapunov exponent. However, instantaneous rates of divergence (which will be denoted by $\lambda(t)$) of neighbouring trajectories can provide useful information about the flow when used in conjunction with the instantaneous spatial structure of the growing perturbation to the flow. For example, calculations of the largest Lyapunov exponent in Taylor–Couette flow (Vastano, Moser & Keefe 1989) showed that when $\lambda(t)$ has a large local maximum, small-amplitude perturbations to the flow only have significant amplitude in the inflow and outflow regions between vortices. In addition these large positive excursions of $\lambda(t)$ only occurred when the inflow and outflow regions were closest together in the spanwise direction, leading Vastano *et al.* (1989) to suggest that a shear instability is responsible for the onset of weak chaos in the Taylor–Couette system.

To examine the physical nature of the temporal chaos observed here in the rotating channel, I have calculated $\lambda(t)$, i.e. instantaneous values of the largest Lyapunov exponent. The method of calculation is dealt with rigorously by Benettin, Galgani & Strelcyn (1976). The flow is perturbed from its fully developed state by a small-amplitude random perturbation. Both the unperturbed and perturbed flows are then advanced in time as described in §2. At $Re = 4.5\,Re_c$ the flow is chaotic so the perturbation grows in time on average; thus, every ten time steps (at this Re one time step is $\Delta t = 0.015d/\bar{U}$) the energy of the perturbation is checked and renormalized to its initial energy level so that it remains a linear perturbation. After a short initial transient period (less than 500 time steps) the initially random perturbation begins to follow a trajectory near the unperturbed flow in solution phase space. The value of $\lambda(t)$ is calculated by taking the log of the ratio of the norm of the perturbation at successive time steps (the norm used here is the L2 norm in Fourier space, i.e. the square root of the sum of the squares of all the Fourier coefficients).
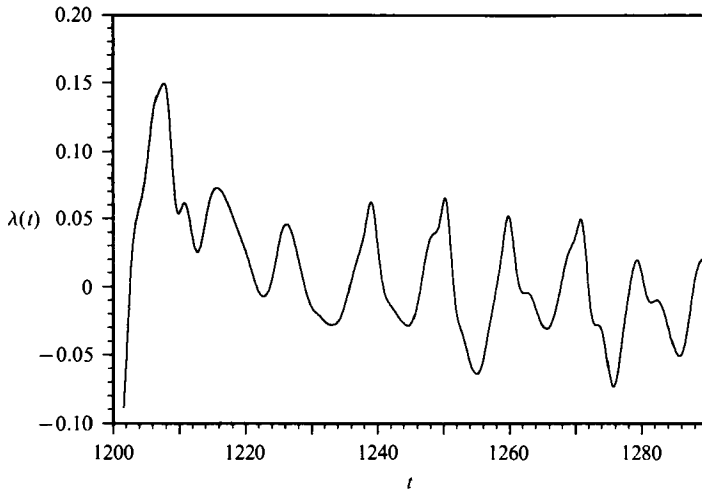
FIGURE 10. A sample of the instantaneous value of the largest Lyapunov exponent $\lambda(t)$ is shown for $Re = 4.5Re_c$.

Several tests of the method for calculating $\lambda(t)$ were performed. For Re in the wavy vortex regime λ should be zero since the flow is temporally periodic (cf. Bergé *et al.* 1984). At $Re = 3.2Re_c$ (which is a wavy vortex flow), $\lambda(t)$ is indeed zero to within truncation and roundoff error. The value of $\lambda(t)$ should also be independent of the amplitude of perturbation, since it is a linear growth rate. Random initial perturbations using the same random seed at $Re = 4.5Re_c$ and having less than 10^{-4} times the energy of the unperturbed flow but varying in energy by a factor of 10000 all yielded the same values of $\lambda(t)$ to within two significant digits. These tests verify the method of calculation of $\lambda(t)$.

Figure 10 shows a portion of $\lambda(t)$ for $Re = 4.5Re_c$. Since $\lambda(t)$ is obtained from a quantity that is averaged over the entire flow (the energy), ω_1 is absent from it, just as for Δp. Much of the energy in $\lambda(t)$ is associated with ω_2' and ω_3, but $\lambda(t)$ is itself temporally chaotic. Different random seeds for the initially random perturbation yielded qualitatively similar $\lambda(t)$ with large maxima and minima occurring at the same times as in figure 10 (to within 1 % of the length of the time shown in figure 10). The time covered by figure 10 is approximately $4T_3$, $4.5T_2'$ or $19T_1$; it therefore covers a time over which significant changes occur in the unperturbed flow.

There are several local maxima having large positive $\lambda(t)$ in figure 10. These are times when the perturbation is diverging most rapidly from the unperturbed flow. Observations of the perturbation at these times show that the perturbation has significant energy only in localized regions. Figure 11 (*a*) shows the kinetic energy of the perturbation in a (y, z)-plane at one streamwise location for $t = 1250.1$. (Figure 10 shows a large maximum of $\lambda(t)$ at this time.) Figure 11 (*b*) shows the streamwise velocity and figure 11 (*c*) shows the cross-flow velocities of the unperturbed flow at the same time and location. The perturbation has significant energy only in two regions close to the $y = -\frac{1}{2}$ wall where the streamwise velocity has largest shear in the spanwise direction (i.e. largest $\partial v_x/\partial z$). These regions are on both sides of the upflow region of the vortices where the vortices bring low-streamwise-velocity fluid away from the wall, creating large spanwise shear on either side of this upflow region. Figure 12 (*a*) shows the kinetic energy of the perturbation in an (x, z)-plane at $y = -\frac{1}{4}$ for the same time as in figure 11. Figure 12 (*b*) shows the streamwise
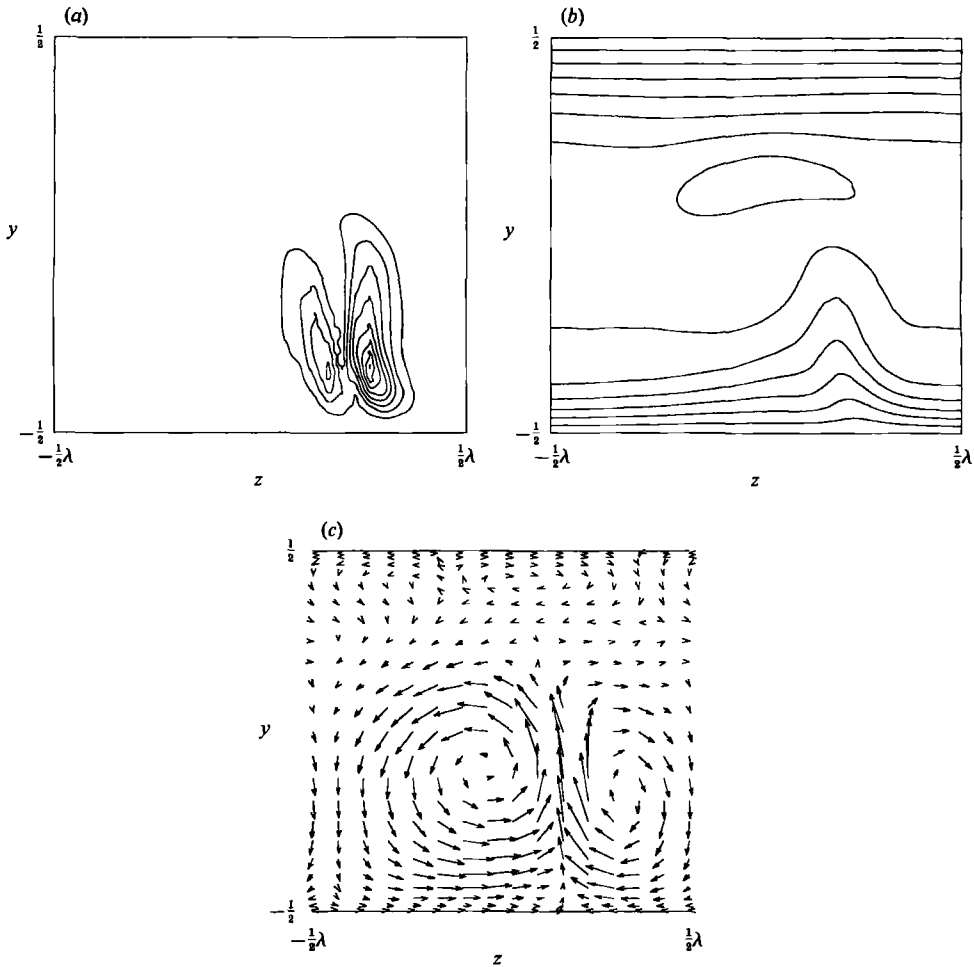
FIGURE 11. For $Re = 4.5 Re_c$ and $t = 1250.1$ (the largest Lyapunov exponent has a large positive value at this time) in a (y, z)-plane at $x = 0$ are shown (a) contours of the kinetic energy of a small-amplitude perturbation to the flow, running from 4×10^{-7} to 32×10^{-7} in increments of 4×10^{-7}; (b) contours of v_x from 0.2 to 1.4 in increments of 0.2; (c) vector plots of the cross-flow velocities v_y and v_z. In (c), velocities are shown only at every second grid point in each direction.

component of velocity for the same time and location. The perturbation is again seen to have significant energy only in the narrow regions on each side of the upflow region where the streamwise velocity has its largest values of spanwise shear. Observations of the perturbation at other times when $\lambda(t)$ has a large positive maximum yield the same conclusion: rapid growth of perturbations occur only in localized regions on each side of the upflow region and near the unstable wall where the streamwise velocity has maximum spanwise shear.

The precise correlation between the spatial location of the maximal spanwise shear of the streamwise velocity and the location of the maximal growth of perturbations suggests that the chaos observed at $Re = 4.5 Re_c$ is driven by instability of these shear regions. (A similar shear instability was proposed by Finlay et al. 1988 as a mechanism for the transition from steady to wavy twisting vortices in the curved channel.) Additional support for shear instability as the physical mechanism behind the chaos observed here is lent by the observation that the magnitude and extent of
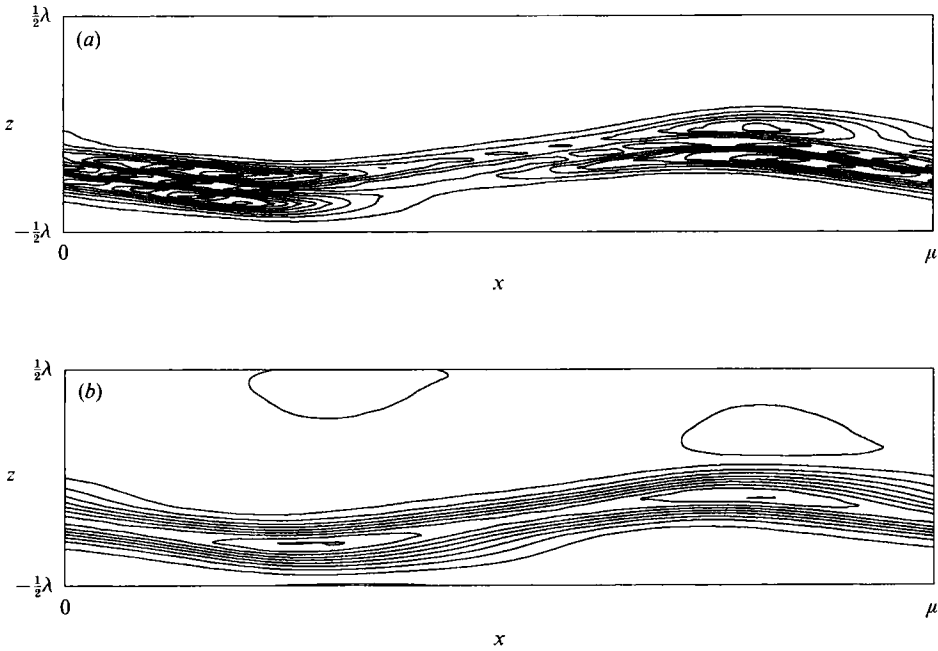
FIGURE 12. For $Re = 4.5 Re_c$ in an (x, z)-plane at $y = -\frac{1}{4}$ and at the same time as figure 11 are shown (a) contours of the kinetic energy of a small-amplitude perturbation to the flow, running from 3×10^{-7} to 30×10^{-7} in increments of 3×10^{-7}; (b) contours of v_x from 0.76 to 1.21 in increments of 0.05.

these shear regions are largest when $\lambda(t)$ is maximum and smallest when $\lambda(t)$ is minimum. For example, plots of v_x in an (x, z)-plane at $y = -\frac{1}{4}$ between $t = 1245$ and 1260 in figure 10 show that the magnitude of the shear is largest when $\lambda(t)$ has a maximum and is on average approximately 15 % larger compared to the minimum values it has when $\lambda(t)$ has a minimum. In addition, these shear regions have maximum spanwise extent when $\lambda(t)$ is maximum, extending approximately 20 % more in the spanwise directions when $\lambda(t)$ is maximum than when it is minimum.

The concentration of the perturbation energy in regions where there is maximal spanwise shear of the streamwise velocity, and the correlation between maximum/minimum magnitude and extent of these shear regions with the times when perturbations diverge most/least rapidly from the unperturbed flow indicate that the chaos observed here is driven by these shear regions. As Re increases, the vortices grow in strength, causing the magnitude of the shear in these regions to increase. Below the onset of chaos, these shear regions are not strong enough on average to cause perturbations to decay on average more than they grow, i.e. to cause the largest Lyapunov exponent to be greater than zero. But above the transition to chaos the growth of perturbations in these shear regions exceed their decay and the resulting flow exhibits the exponential divergence, on average, of neighbouring trajectories associated with chaos.

7. Turbulent rotating channel flow

When Re is increased to $6.7 Re_c$, temporal spectra show a broadband spectrum, as shown in figure 13. This run was started from the random initial conditions discussed in §2. The flow is no longer just wavy vortices modulated by a few frequencies or
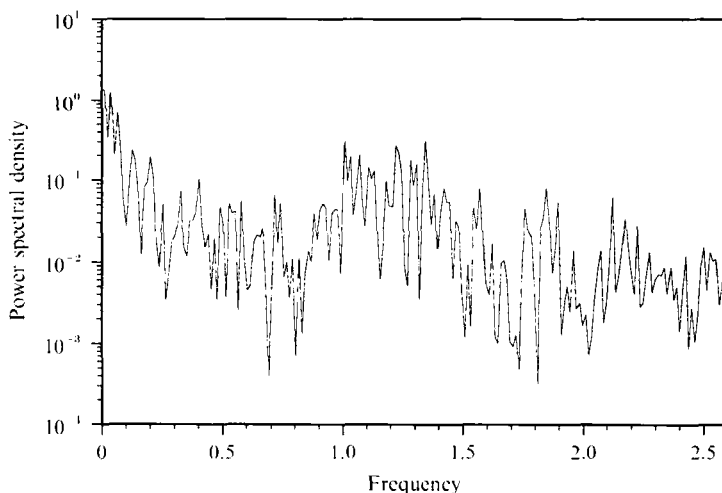
FIGURE 13. Power spectral density of v_z for mildly turbulent vortices at $Re = 6.7\,Re_c$ sampled at one point in the flow. The flow has reached its equilibrium state prior to sampling.

weak chaos. The fundamental frequencies $\omega_1, \omega_2', \omega_3$ may still be present, but they are masked by a continuous spectrum of frequencies having equal or greater energy.

In some systems, inadequate resolution produces broadband energy in temporal spectra that disappears in properly resolved simulations (Curry et al.1984). Spatial energy spectra shown in figure 14 for $t = 1000$ show the $32 \times 20 \times 20$ resolution used here is adequate since these spectra decay exponentially up to the highest wavenumbers resolved. Further details of the data in figure 14 are given in the Appendix. There is a mild slowing of the decay rate at the highest wavenumber in $14(a)$ and $14(c)$, but no upturn or oscillation in the spectra associated with inadequate resolution.

Instantaneous flow fields at $Re = 6.7\,Re_c$ show that the major flow feature is still a pair of streamwise-oriented vortices. However, the flow has lost the shift-and-reflect symmetry that was present at lower Re (in the absence of spanwise travelling). This is evident in figure 15, where v_x in an (x, z)-plane at $y = -0.416$ is shown for $t = 1003.75d/\bar{U}$. The upflow boundary near $z = 0$ no longer has the symmetric S-shape that it had at lower Re; its appearance varies chaotically in time. Observations of the flow at different times also show that the pair of vortices now moves chaotically about in the spanwise direction, with excursions of $\pm\frac{1}{2}$ times the vortex spacing not uncommon. The location of the primary vortices also varies chaotically up and down in the y-direction in time as well as in the streamwise direction. Occasionally at some streamwise locations one vortex lies almost directly above the other in y, with the 'upflow' region directed almost entirely spanwise, while at the same time and at other streamwise locations the primary vortices are in their more usual side-by-side state. Chaotic motion was observed by Johnston Halleen & Lezius (1972) at much higher Re, but was thought to be due to experimental noise or finite-span effects. Neither of these are present in the current simulation; the chaotic motion of the vortices is inherent in the dynamical system. Using reflective flakes to visualize the upflow and downflow regions of the vortices, Alfredsson & Persson (1989) also observe vortices whose upflow and downflow regions move about chaotically and appear turbulent at the same $Re = 590$ as here, although they provide no observations at the higher Ro used here.
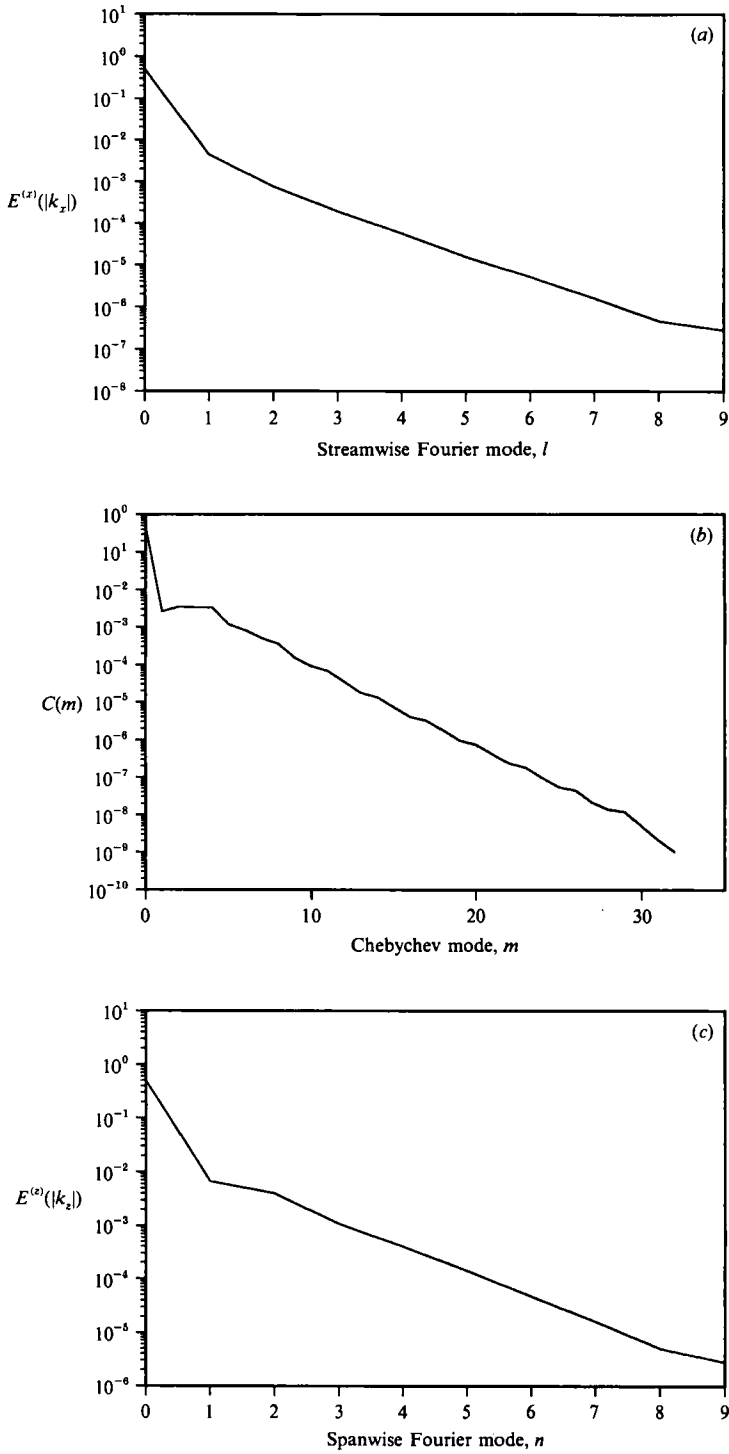
FIGURE 14. The energy of the flow as a function of (a) streamwise Fourier mode (b) Chebyshev mode (in the y-direction) and (c) spanwise Fourier mode, for $t = 1000$ and $Re = 6.7\,Re_{\rm c}$. See the Appendix for definition of quantities.
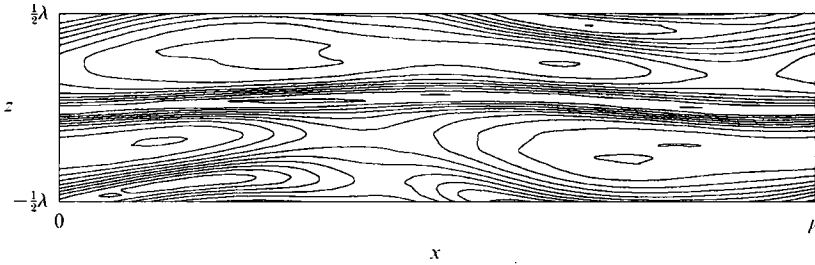
FIGURE 15. Contours of v_x for $Re = 6.7\,Re_c$ at $t = 1003.75$ and $y = -0.416$, running from 0.345 to 0.925 in increments of 0.058.
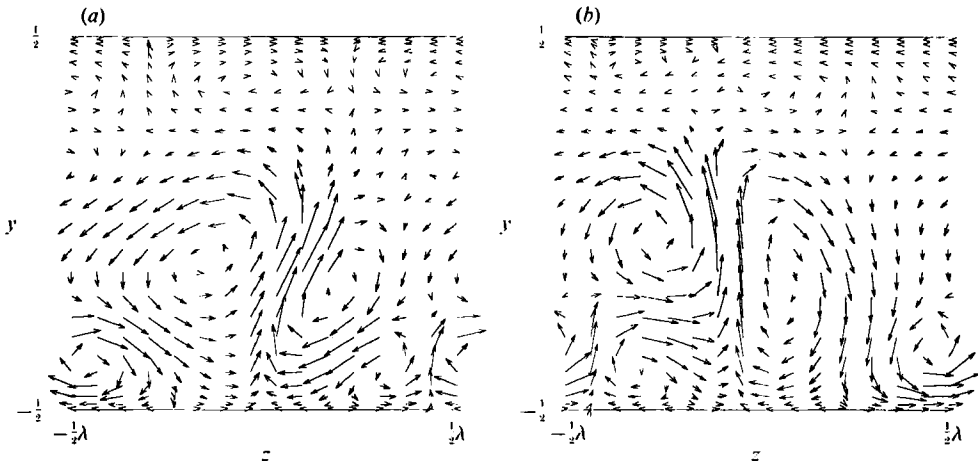

FIGURE 16. Vector plots of the cross-flow velocities v_y and v_z are shown for $Re = 6.7\,Re_c$ at the same time as figure 15 and for (a) $x = 0.133$ and (b) $x = 0.7$. Velocities are shown only at every second grid point in each direction.

7.1. *Quasi-coherent structures*

Instantaneous flow fields also show that in addition to the primary vortex pair, secondary streamwise-oriented vortices of limited streamwise extent sometimes appear near the unstable $(y = -\frac{1}{2})$ wall. Observations of the flow at other times show that these secondary vortices are transient and occur at irregular intervals in time. They also appear sometimes as a single vortex instead of a pair. Figure 16 shows vector plots of the cross-flow velocity for two (y, z)-planes for the same flow as shown in figure 15. Counter-rotating secondary vortex pairs are centred near $z = \pm\frac{1}{2}\lambda$. In the terminology used to describe the quasi-coherent structures that occur in turbulent boundary layers, these secondary vortices cause sweeps and ejections in conjunction with low-speed streaks. The secondary vortices eject low-velocity fluid away from the wall and sweep high-velocity fluid toward the wall, causing the high-velocity regions on either side of the primary upflow region and the low-velocity regions near $z = \pm\frac{1}{2}\lambda$ (low-speed streaks) in figure 15.

The size, location, and flow patterns of these secondary vortices are similar to those of the quasi-coherent structures observed in turbulent boundary layers. Instantaneous flow fields associated with ten different secondary vortex structures were obtained. The spanwise period of the computational domain is $81\nu/u_\tau$, i.e. 81 wall units $(u_\tau^2 = \tau/\rho$, where τ is the time-average streamwise shear stress on the

unstable wall). Since only one structure was ever observed per spanwise period, the spanwise spacing of the secondary vortices is 81 wall units, which is the most probable spacing of the wall-layer structures observed in turbulent boundary layers (Cantwell 1981). The streamwise extent of the secondary vortices is on average approximately $176 \, \nu/u_\tau$ (individual structures vary by up to $\pm 40\%$ from this average and the streamwise extent of the computational region is 326 wall units). The streamwise length of the vortices is thus in the range 100–2000 for sublayer structures observed in turbulent boundary layers (Cantwell 1981). In wall units, the secondary vortex centres are on average located near approximately $y^+ = 12$ (according to Cantwell 1981, the centre of the streamwise vortices observed in turbulent boundary layers varies from $10 \, \nu/u_\tau$ to $25 \, \nu/u_\tau$ with $15 \, \nu/u_\tau$ about average). The secondary vortices observed here thus produce instantaneous flow fields that have sweeps, ejections, streaks and vortical structures of the same size and location as those associated with these coherent structures in the turbulent boundary layer. The relation between streamwise-oriented vortical structures in the sublayer and streaks, sweeps and ejections has not yet been entirely sorted out in the flat-plate turbulent boundary layer (Robinson 1991), but simulations of the flat-plate boundary layer (Robinson, Kline & Spalart 1988) show a strong spatial association between vortical structures and ejections, sweeps, and low-speed streaks. The transient secondary vortices observed here are believed to be the same type of quasi-coherent sublayer vortex structures as observed in the flat-plate boundary layer.

Of the ten secondary vortex structures observed for a small portion of their life, all were counter-rotating pairs of vortices when at maximum strength, although often for part of their life one of the vortices is much weaker than the other or even absent. Nine of the ten pairs observed had the same sense of vorticity as the primary pair in the sense that the distance between vortex centres was much less across their upflow region.

The life history of four different secondary vortex structures was also determined. Two of these structures that were followed in time first appeared close to the unstable wall in the downflow region between the primary vortices. One of these two appeared first as a weak single vortex but soon became a vortex pair, while the other first appeared as a weak vortex pair. These two structures then moved away from the wall as they grew in strength. The secondary vortex centres reached a maximum distance from the wall of approximately $12 \, \nu/u_\tau$ when the secondary vortices were strongest. The structures then decayed as they moved toward the wall. For both of these events, one of the vortices decayed much more rapidly than the other, leaving a single decaying weak vortex over most of the latter third of the life of the structure. The life of these two structures was approximately 200 viscous time units, although for most of this time they were very weak. The secondary vortices have secondary velocities of the same magnitude as the primary vortices for only about 50 viscous time units, which is the same length of time that strong coherent structures associated with sublayer vortices are found in simulations of turbulent plane channel flow (Guezennec, Piomelli & Kim 1989). The secondary vortices are convected in the downstream direction at a speed approximately equal to the mean streamwise velocity at the average y-location of their centres, as is also found in the turbulent plane channel (Guezennec *et al.* 1989).

The other two secondary vortex structures observed over time were both born near the unstable wall in the upflow region between the primary vortices. These two structures grew much more rapidly than those born in the downflow region, growing to maximum strength within approximately 20 viscous time units (compared with 50

or so viscous time units for the two structures born in the downflow region). Very soon after reaching a strength near that of the primary vortices, each of these two upflow structures merged rapidly with the primary vortices, producing primary vortices with large extent in the y-direction. This merger occurred over about 20 viscous time units as well, so the entire life of each of these two upflow events was approximately 40 viscous time units. Secondary vortices which form in the upflow region between the primary pair would not be expected to last long since the primary vortices induce strong motion away from the wall there. Only three of the ten structures observed instantaneously were near the upflow region. However, at much higher Re, Johnston et al. (1972) observed more low-speed streaks in the upflow region compared to the downflow region, which is opposite to what might be expected from the short life and smaller number of upflow events observed here. This difference may be caused by the much lower Re used here so that the sublayer structures have size almost equal to that of the primary vortices and therefore interact strongly with the primary vortices. Any upflow events are quickly swept away from the wall. At high Re the sublayer is much smaller and the associated structures would not interact so strongly with the primary vortices.

In experiments (Johnston et al. 1972) and large-eddy simulations (Tafti & Vanka 1991) it is also found that rotation reduces the number of coherent structures observed near the stabilized wall. In agreement with this, no secondary vortex structures occur near the stable wall ($y = \frac{1}{2}$) here. Although the flow near the stable wall in the simulation at $Re = 6.7 Re_c$ does not have turbulent structures present, it is still temporarily chaotic. However, the secondary velocities here are small.

The appearance of coherent structures could be associated with the rapid growth of disturbances in the flow in the local region where the coherent structure develops. If this were true then the instantaneous largest Lyapunov exponent should have a large positive maximum when coherent structures develop. Similarly, when coherent structures form, perturbations to the flow should grow in regions where the coherent structures appear. These statements can be tested by calculating the largest Lyapunov exponent $\lambda(t)$ and observing the spatial character of the perturbation flow, as described in the previous section. Such calculations show there is no correlation between maxima or minima of $\lambda(t)$ and the appearance or disappearance of secondary vortex structures. Instead, large maxima and minima of $\lambda(t)$ are correlated with maxima and minima of the magnitude of the spanwise shear occurring on either of the upflow region of the primary pair of vortices, just as discussed in the previous section for weakly chaotic flow at $Re = 4.5 Re_c$. Large maxima in $\lambda(t)$ occur when no secondary vortices are present, and secondary vortices do not necessarily form after a large maxima in $\lambda(t)$. Similarly, secondary vortex structures appear without any maxima in $\lambda(t)$ occurring prior to or during their formation, and secondary vortices were observed to live their life over a period when $\lambda(t)$ is near a large negative minimum. When no structures are present at the time when $\lambda(t)$ has a large positive maximum, perturbations to the base flow are found to have significant energy only in the same localized regions of large spanwise v_x shear on either side of the upflow region near $y = -\frac{1}{2}$ as found for $Re = 4.5 Re_c$. Since secondary vortices are often born in the downflow region where perturbations from the base flow do not grow, the appearance of these secondary vortices is not associated with the local growth of the perturbation. When a pair of secondary vortices is present at the time when $\lambda(t)$ has a large positive maximum, then the upflow region of the structure causes additional spanwise shear regions where the perturbation has significant energy. For example, figure 17(a) shows cross-flow
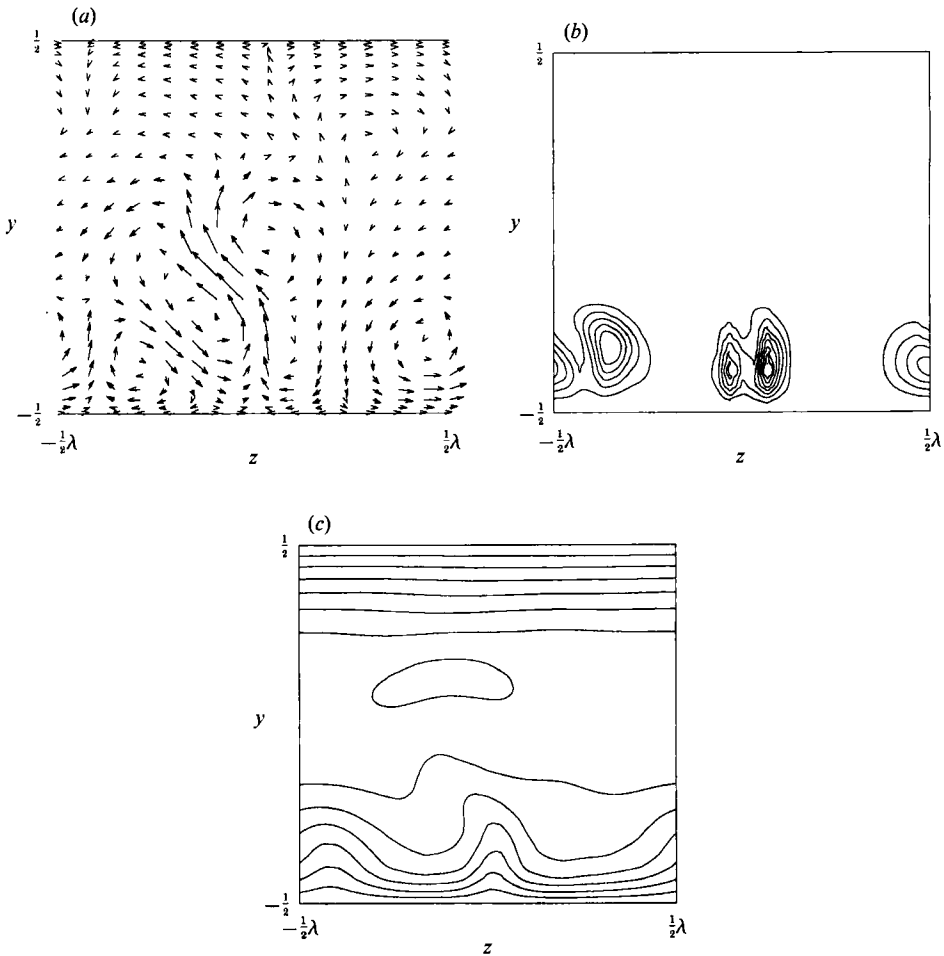
FIGURE 17. For $Re = 6.7 Re_c$, $t = 1038.5$ and $x = 0.2$ are shown (a) vector plots of the cross-flow velocities v_y and v_z; (b) contours of the kinetic energy of a small-amplitude perturbation to the flow, running from 1×10^{-6} to 8×10^{-6} in increments 1×10^{-6}; (c) contours of v_x from 0.2 to 1.4 in increments of 0.2.

velocities in a (y, z)-plane at a time when $\lambda(t)$ has a large positive maximum and at a streamwise location where secondary vortices are present. The kinetic energy of the corresponding perturbation flow is shown in figure 17(b) and is seen to be significant only in the primary and secondary upflow regions of significant $\partial v_x / \partial z$ seen in figure 17(c). The secondary vortices thus contribute to the chaos by causing $\partial v_x / \partial z$, but are not produced by the spanwise shear that drives the chaos. Since the coherent structures observed here are not produced by the local growth of perturbations, then they may, for example, be due to the appearance of a heteroclinic or homoclinic connection as found in the simple model of boundary-layer coherent structures described by Aubry *et al.* (1988).

7.2. *Time-average profiles*

For a quantity $v(x, y, z, t)$, the time-average profile was obtained in the standard way by spatially averaging v at fixed y over the periodic x- and z-directions and then averaging over time, producing the quantity $\bar{v}(y)$. When plotted in wall units, the

mean velocity profile $\bar{u}^+ = \bar{u}/u_\tau$ satisfies the viscous sublayer linear relation $\bar{u}^+ = y^+$ near both walls and for all Re. For $y^+ < 3$, $\bar{u}^+/y^+$ differs by less than 8% from 1.0. The law of the wall, however, is not satisfied because Re is so low. In wall units, the region $y < 0$ occupies less than 40 wall units at $Re = 6.7Re_c$. The middle of the channel would be only marginally out of the buffer layer if this were a fully turbulent boundary layer. As a result, the law of the wall is not valid at all at such a low Re. The turbulent processes responsible for the log-law relation are not present here.

At much higher Re ($Re = 11\,500$ and $Re = 35\,000$), and at lower Ro ($Ro \leqslant 0.21$) than here, Johnston et al. (1972) find that the mean streamwise velocity profile, $\bar{u}(y)$ has a region where $\partial \bar{u}/\partial y = 2Ro$ and so the flow in this region is inviscidly neither stable nor unstable. (The inviscid criterion for instability in the rotating channel is $\partial \bar{u}/\partial y - 2Ro > 0$, cf. Tritton & Davies 1985.) Close examination of the data shows that there is no such region of constant $\partial \bar{u}/\partial y$, and that $\partial \bar{u}/\partial y = 2Ro$ only at one y-location (near $y = 0$), not a range of y as found by Johnston et al. (1972).

Time-averaged profiles of the fluctuating velocities show that the transient secondary vortices cause velocity fluctuations that are up to 30% greater than at lower Re. The secondary vortices also cause increased mixing of momentum near the unstable wall, resulting in mean velocity profiles that are approximately 10% greater in the region where the secondary vortices occur. The total shear stress profile varies linearly with y for all three Re.

8. Concluding remarks

Direct numerical simulation was used to examine the flows leading up to turbulence in a rotating channel as the Reynolds number is increased. For the rotation rate $Ro = 0.5$ used here, the first transition with Re increasing beyond that for temporally periodic wavy vortices results in a second frequency, ω_2, appearing in the flow. For all Reynolds numbers, wavenumbers and initial conditions where this flow was observed this frequency is not incommensurate; instead, it is locked with the wavy vortex frequency in a ratio that depends on the parameters. Physically this new frequency corresponds to slow spanwise motion of the vortices (in addition to the streamwise motion of the wavy vortex waves).

At higher Re near $4.1Re_c$, ω_2 is replaced by a new frequency, ω_2', in the flow that produces a modulated wavy vortex flow similar in some ways to modulated wavy Taylor vortex flow. Unlike the Taylor–Couette geometry, this modulation frequency can frequency lock with the travelling wave frequency. Near $Re = 4.2Re_c$, a third frequency appears, yielding a quasi-periodic flow with three incommensurate frequencies. At $Re = 4.5Re_c$ temporal chaos is present. The flow is not turbulent though, since no small-scale structures are present. Calculations of the instantaneous largest Lyapunov exponent show that perturbations to the flow grow most/least rapidly when the spanwise-shear regions of the streamwise velocity component on either side of the upflow region are strongest/weakest. In addition, the spatial structure of small perturbations to the flow are found to have significant value only in these same localized spanwise-shear regions. The chaos occurring at this Re thus appears to be driven by spanwise shear instability of the streamwise velocity component.

At $Re = 6.7Re_c$ ($Re = 590$), quasi-coherent structures exist near the high-pressure (inviscidly unstable) wall of the channel in the form of transient, secondary streamwise-oriented vortices like those observed in other turbulent boundary layers. The primary vortices remain in the flow, but move about chaotically. The secondary

vortices sometimes interact with the primary vortices. The disordered appearance of the reflective flake visualizations of Alfredsson & Persson (1989) at $Re = 590$ but at lower Ro is probably caused by these secondary vortex structures coupled with the disordered motion of the primary vortices.

Despite the presence of turbulent boundary-layer structures at $Re = 6.7\,Re_c$, time-average velocity and shear stress profiles are qualitatively determined by the primary vortices, with relatively small quantitative effects caused by the secondary vortex structures. The mean velocity profile is linear in the viscous sublayer at all Re considered. However, for the low-Re turbulent channel ($Re = 6.7\,Re_c$) the mean velocity profile does not obey the turbulent log-law relation since the entire boundary layer on the high-pressure side occupies less than 40 wall units.

Calculations of the instantaneous largest Lyapunov exponent for the flow at $Re = 6.7\,Re_c$ show that the occurrence of the quasi-coherent secondary vortex structures is not due to the growth of small perturbations to the flow. In addition, observations of the spatial structure of small perturbations to the flow show that such perturbations grow only in the same regions as for the non-turbulent chaotic flow observed at $Re = 4.5\,Re_c$, i.e. in the regions of largest spanwise shear of the streamwise velocity component that occur on either side of the upflow region. The quasi-coherent structures do not usually form here. Thus these structures are not the result of the local growth of small disturbances to the flow, but may instead be associated with the appearance of a homoclinic or heteroclinic connection in phase space.

Appendix

The data in figure 14(a) show

$$E^{(x)}(k_x) = c(k_x) \int_{-\frac{1}{2}}^{\frac{1}{2}} \sum_{n=0}^{10} [|\hat{v}(y, k_x, k_z, t)|^2 + [|\hat{v}(y, k_x, -k_z, t)|^2 \, \mathrm{d}y, \qquad (A\,1)$$

where $k_x = 1\beta$ and $k_z = n\alpha$. Figure 14(c) shows

$$E^{(z)}(k_z) = c(k_z) \int_{-\frac{1}{2}}^{\frac{1}{2}} \sum_{l=0}^{10} [|\hat{v}(y, k_x, k_z, t)|^2 + [|\hat{v}(y, -k_x, k_z, t)|^2 \, \mathrm{d}y, \qquad (A\,2)$$

where

$$c(k) = \begin{cases} \frac{1}{2} & (k = 0) \\ 1 & (k \neq 0) \end{cases}, \qquad (A\,3)$$

and $\hat{c}(y, k_x, k_z, t)$ is the discrete Fourier transform (in x and z) of the velocity, defined as

$$v(x, y, z, t) = \sum_{l=-10}^{10} \sum_{n=-10}^{10} \hat{v}(y, k_x, k_z, t) \exp{(\mathrm{i}k_x x)} \exp{(\mathrm{i}k_z z)}. \qquad (A\,4)$$

Figure 14(b) shows the magnitude of the Chebyshev coefficients $|a(m)|^2$ in the representation

$$v(x, y, z, t) = \sum_{m=0}^{32} a(m, y, z, t) \, T_m(y), \tag{A5}$$

where T_m is the usual mth Chebyshev polynomial.

REFERENCES

ALFREDSSON, P. A. & PERSSON, H. 1989 Instabilities in channel flow with system rotation. *J. Fluid Mech.* **202**, 543.

ARNOLD, V. I. 1965 Small denominators I. Mappings of the circumference onto itself. *Am. Math. Soc. Transl.* **46**, 213.

AUBRY, N., HOLMES, P. LUMLEY, J. L. & STONE, E. 1988 The dynamics of coherent structure in the wall region of a turbulent boundary layer. *J. Fluid Mech.* **192**, 115.

BENETTIN, G., GALGANI, L. & STRELCYN, J. 1976 Kolmogorov entropy and numerical experiments. *Phys. Rev.* A **14**, 2338.

BERGÉ, P., POMEAU, Y. & VIDAL, C. *Order Within Chaos.* John Wiley & Sons.

BIRINGEN, S. & PELTIER, L. J. 1990 Numerical simulation of 3-D Bénard convection with gravitational modulation. *Phys. Fluids* A **2**, 754.

BLAND, S. B. & FINLAY, W. H. 1991 Transitions toward turbulence in a curved channel. *Phys. Fluids* A **3**, 106.

CANTWELL, B. J. 1981 Organized motion in turbulent flow. *Ann. Rev. Fluid Mech.* **13**, 457.

CANUTO, C., HUSSAINI, M. Y., QUARTERONI, A. & ZANG, T. A. 1988 *Spectral Methods in Fluid Dynamics.* Springer.

COUGHLIN, K. T. 1990 Quasiperiodic Taylor–Couette flow. Ph.D. thesis. Harvard University.

COUGHLIN, K. T. & MARCUS, P. S. 1992a Modulated waves in Taylor–Couette flow. Part 1. Analysis. *J. Fluid Mech.* **234**, 1.

COUGHLIN, K. T. & MARCUS, P. S. 1992b Modulated waves in Taylor–Couette flow. Part 2. Numerical simulation. *J. Fluid Mech.* **234**, 19.

CURRY, J. H., HERRING, J. R., LONCARIC, J. & ORSZAG, S. A. 1984 Order and disorder in two- and three-dimensional Bénard convection. *J. Fluid Mech.* **147**, 1.

FENSTERMACHER, P. R., SWINNEY, H. L. & GOLLUB, J. P. 1979 Dynamical instabilities and the transition to chaotic Taylor vortex flow. *J. Fluid Mech.* **94**, 103.

FINLAY, W. H. 1989 Perturbation expansion and weakly nonlinear analysis for two-dimensional vortices in curved or rotating channels. *Phys. Fluids* A **1**, 854.

FINLAY, W. H. 1990 Transition to oscillatory motion in rotating channel flow. *J. Fluid Mech.* **215**, 209–227.

FINLAY, W. H., KELLER, J. B. & FERZIGER, J. H. 1988 Instability and transition in curved channel flow. *J. Fluid Mech.* **194**, 417.

FINLAY, W. H. & NANDAKUMAR, K. 1990 Onset of two-dimensional cellular flow in finite curved channels of large aspect ratio. *Phys. Fluids* A **2**, 1163.

GOLLUB, J. P. & BENSON, S. V. 1980 Many routes to turbulent convection. *J. Fluid Mech.* **100**, 449.

GORMAN, M. & SWINNEY, H. L. 1982 Spatial and temporal characteristics of modulated waves in the circular Couette system. *J. Fluid Mech.* **117**, 123.

GUEZENNEC, Y. G., PIOMELLI, U. & KIM, J. 1989 On the shape and dynamics of wall structures in turbulent channel flow. *Phys. Fluids* A **1**, 764.

GUO, Y. & FINLAY, W. H. 1991 Splitting, merging and wavelength selection of vortices in curved and/or rotating channels due to Eckhaus instability. *J. Fluid Mech.* **228**, 661.

HALL, P. 1988 The nonlinear development of Görtler vortices in growing boundary layers. *J. Fluid Mech.* **193**, 243.

HERBERT, TH. 1988 Secondary stability of boundary layers. *Ann. Rev. Fluid Mech.* **20**, 487.

JIMÉNEZ, J. 1990 Transition to turbulence in two-dimensional Poiseuille flow. *J. Fluid Mech.* **218**, 265.

JIMÉNEZ, J. & MOIN, P. 1991 The minimal flow unit in near-wall turbulence. *J. Fluid Mech.* **225**, 213.

JOHNSTON, J. P., HALLEEN, R. M. & LEZIUS, D. K. 1972 Effects of spanwise rotation on the structure of two-dimensional fully developed turbulent channel flow. *J. Fluid Mech.* **56**, 533.

KLEISER, L. & ZANG, T. 1991 Numerical simulations of transition in wall-bounded flows. *Ann. Rev. Fluid Mech.* **23**, 495.

KUZ'MINSKII, L. V., SMIRNOV, E. M. & YURKIN, S. V. 1983 Longitudinal cellular structures of Taylor–Görtler type vortices on the high-pressure side of rotating channels. *J. Appl. Mech. Tech. Phys.* **24**, 882.

MALIK, M. R. & HUSSAINI, M. Y. 1990 Numerical simulation of interactions between Görtler vortices and Tollmien–Schlichting waves. *J. Fluid Mech.* **210**, 183.

MATSSON, O. J. & ALFREDSSON, P. H. 1990 Curvature- and rotation-induced instabilities in channel flow. *J. Fluid Mech.* **210**, 537.

MOSER, R. D., MOIN, P. & LEONARD, A. 1983 A spectral numerical method for the Navier-Stokes equations with applications to Taylor–Couette flow. *J. Comput. Phys.* **52**, 524.

OLINGER, D. J. & SREENIVASAN 1988 Nonlinear dynamics of the wake of an oscillating cylinder. *Phys. Rev. Lett.* **60**, 797.

RAND, D. 1982 Dynamics and symmetry. Predictions for modulated waves in rotating fluids. *Arch. Rat. Mech. Anal.* **79**, 1.

REED, H. L. 1988 Wave interactions in swept-wing flows. *Phys. Fluids* **30**, 3419.

ROBINSON, S. K. 1991 Coherent motions in the turbulent boundary layer. *Ann. Rev. Fluid Mech.* **23**, 601.

ROBINSON, S. K., KLINE, S. J. & SPALART, P. R. 1988 Quasi-coherent structures in the turbulent boundary-layer: Part II. Verification and new information from a numerically simulated flat-plate layer. In *Near-Wall Turbulence* (ed. S. J. Kline & N. H. Afgan), p. 218. Hemisphere.

SMIRNOV, E. M. & YURKIN, S. V. 1983 Fluid flow in a rotating channel of square section. *Fluid Dyn.* **18**, 850.

TAFTI, D. K. & VANKA, S. P. 1991 A numerical study of the effects of spanwise rotation on turbulent channel flow. *Phys. Fluids* A **3**, 642.

TRITTON, D. J. & DAVIES, P. A. 1985 Instabilities in geophysical fluid dynamics. In *Hydrodynamic Instabilities and the Transition to Turbulence* (ed. H. L. Swinney & J. P. Gollub), p. 229. Springer.

TRYGGVASON, G. & UNVERDI, S. O. 1990 Computations of three-dimensional Rayleigh–Taylor instability. *Phys. Fluids* A **2**, 656.

VASTANO, J. A., MOSER, R. D. & KEEFE, L. 1989 A proposed mechanism for the transition to chaos in Taylor–Couette flow. *Bull. Amer. Phys. Soc.* **34**, 2264.

YANG, K.-S. & KIM, J. 1991 Numerical investigation of instability and transition in rotating plane poiseuille flow. *Phys. Fluids* A **3**, 633.